IOP Publishing Superconductor Science and Technology
Supercond. Sci. Technol. 33 (2020) 034010 (9pp) https://doi.org/10.1088/1361-6668/ab6ebf

# Secondary phase particles in bulk, infiltration-growth processed YBCO investigated by transmission Kikuchi diffraction and TEM

**A Koblischka-Veneva[1,2], M R Koblischka[1,2], J Schmauch[2] and M Murakami[1]**

[1] Superconducting Materials Laboratory, Department of Materials Science and Engineering, Shibaura Institute of Technology, Tokyo 135-8548, Japan
[2] Experimental Physics, Saarland University, PO Box 151150, D-66041 Saarbrücken, Germany

E-mail: anjela@shibaura-it.ac.jp

Received 30 September 2019, revised 19 December 2019
Accepted for publication 22 January 2020
Published 12 February 2020


**Abstract**

We present results of the first application of the transmission Kikuchi diffraction (TKD) technique to bulk, infiltration growth (IG)-processed $YBa_2Cu_3O_{7-\delta}$ (YBCO) superconductors with embedded $Y_2BaCuO_5$(Y-211) nanoparticles. By means of focused ion-beam (FIB) milling, TEM slices were prepared from mechanically polished surfaces of bulk, IG-processed YBCO samples. The required optical transparency was reached by additional polishing the resulting surfaces using the FIB and Ar-ion milling. For TKD, the sample was mounted on a homebuilt sample holder in the SEM, which provides the required inclination for TKD. The improved spatial resolution of TKD enabled the investigation of the small Y-211 particles (diameter of about 60–210 nm) embedded in the superconducting YBCO matrix. The fabricated TEM slices further enable the application of transmission electron microscopy to the same sample sections. These tiny Y-211 particles embedded within the YBCO matrix are, together with their strain fields, directly responsible for the high irreversibility fields due to the effective flux pinning of the IG-processed samples.

Keywords: YBCO, EBSD, infiltration growth, microstructure

(Some figures may appear in colour only in the online journal)

## 1. Introduction

For the growth of single-crystalline, bulk superconductor samples of $YBa_2Cu_3O_x$(YBCO or Y-123), the melt-texturing technique was developed using a seed crystal on top of the bulk, pressed from precursor powder material [1]. This so-called melt-texture, melt-growth (MTMG) technique and its derivates can produce well-textured superconductor samples with well developed critical current densities, $j_c$, to be applied for magnetic bearings or trapped field (TF) magnets ('super-magnets'). The record values achieved for the TFs are 17.6 T at 26 K and 17.2 T at 29 K [2, 3]. The improvement of the sample microstructures to obtain an homogeneous distribution of small-sized (ideally $r \sim 2\xi$ with $\xi$ being the Cooper pair diameter [4]) pinning centres from the secondary phase $Y_2BaCuO_5$(Y-211) is still a central issue for research on these materials. However, there is another drawback of the MTMG approach: the uncontrolled shrinkage of the original pellet [5]. Due to these problems, another approach was introduced as early as 1991 [6–10]; the so-called infiltration growth (IG) technique. Here, a Y-211 precursor pellet is formed which is then used as a base material together with a liquid source and a seed crystal. As result, there is no shrinkage effect, and it becomes possible to design the shape of the superconductor sample. In the recent years, the IG-technique got several improvements as reviewed in [11], but

 

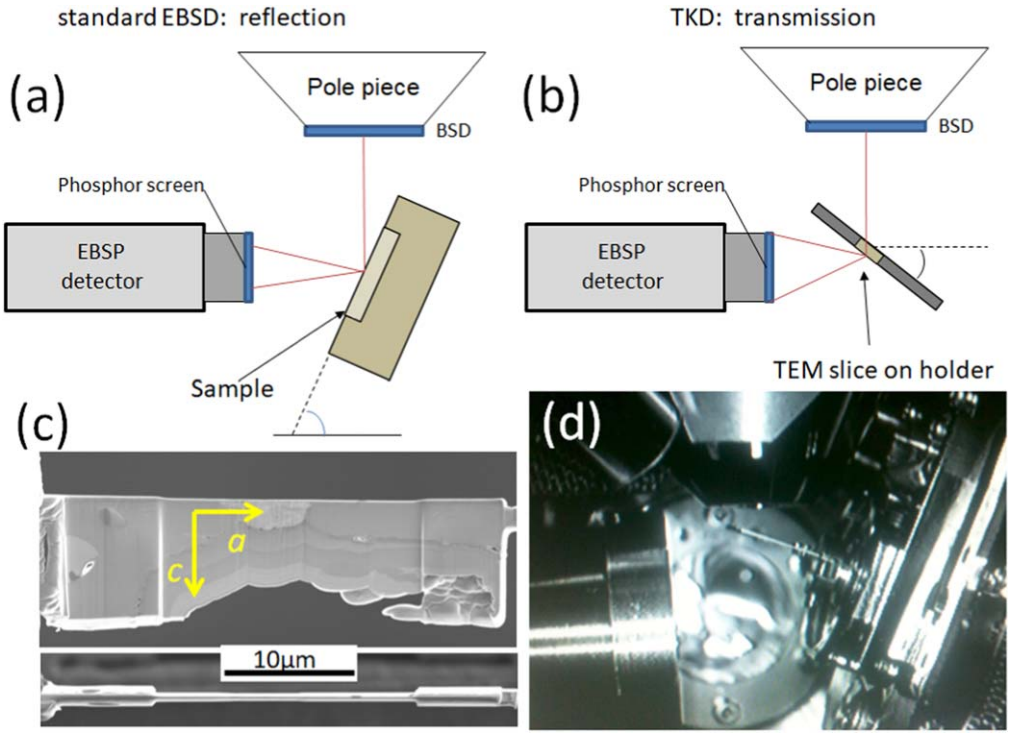


**Figure 1.** Schematic drawings of conventional EBSD (a) and TKD (b). Also indicated are the sample inclination angles required for EBSD imaging. (c) Presents SEM views of the ready TEM slice fixed on the micromanipulator—the surface for analysis (top) and the cross-section (bottom). The crystallographic orientation is also indicated. Finally, (d) shows the home-built TEM slice holder for TKD imaging mounted in the SEM chamber.

the investigations of the physical properties of the IG-processed bulks in the literature have revealed that the resulting irreversibility fields, $H_{irr}$, are very large, but the $j_c$-values have not yet reached the ones of the MTMG-samples. A recent work could, however, demonstrate a record TF value of 14.3 T at 28 K [12].

Therefore, it is an essential issue to investigate and understand the specific microstructure of the IG-processed YBCO samples in detail. To perform microscopic imaging of the embedded flux pinning sites in the nanometre range, the most modern techniques are required. The electron backscatter diffraction (EBSD) technique has proven to be a very useful tool, mostly on metallic samples, and more recently, also on various ceramic sample types [13–16]. However, the standard EBSD technique suffers from distinct problems like charging effects, which hinder the observation of nanometre-sized grains. Therefore, the transmission Kickuchi diffraction (TKD) technique was very recently developed by several authors [17–19] with the goal to improve the spatial resolution of EBSD on such materials. The arrangement of the electron beam and the sample for standard EBSD and TKD is illustrated in figures 1(a) and (b). As result, the spatial resolution could be improved from several tens of nanometres to ~5–10 nm, depending on the material to be studied [20, 21]. Furthermore, the effects of charging in non-conducting samples are considerably reduced, which is a great advantage for the investigation of various ceramic materials as well as biomaterials [22]. This allowed already for TKD investigations on $MgB_2$ [23, 24] as well as YBCO [25].

## 2. Experimental procedures

### *2.1. Sample and surface preparation, TEM slices*

The IG-processed samples were prepared as described in [26]. Samples with a diameter of 20 mm and a height of 8 mm using the IG process at various growth temperatures, i.e. 990 °C, 985 °C, 983 °C, 980 °C and 978 °C and a common holding time of 25 h. The temperature programme was based on thermogravimetric analysis. The samples were heated up at a rate of 100 °C $h^{-1}$ to the temperature of 880 °C and kept there for 15 min, again heated up in 0.5 h to the final reaction temperature of 1040 °C and kept there for 50 min. Then, the temperature was reduced in 60 min to 1000 °C, and further slowly decreased by another 25 °C with a cooling rate of 0.3 °C $h^{-1}$. Finally, the temperature was reduced at a cooling rate of 100 °C $h^{-1}$ to 100 °C and then, the furnace was left to cool down to room temperature. The melt-textured samples were annealed at 450 °C for 150 h in flowing pure oxygen gas.

The as-prepared pellets were cut 3 mm below the seed as illustrated in figure 2(a). The resulting surfaces were mechanically polished using $SiO_2$ grinding papers and diamond paste, followed by a polishing step using OP-S colloidal solution (Struers) with 40 nm particles, and using only ethanol as a lubricant [16]. Then, these sample surfaces were investigated by SEM and EBSD (standard configuration) in order to select the best-suited area for milling out a TEM slice. The location of the area studied is also indicated in figure 2(b), where also the growth sectors of the IG-sample

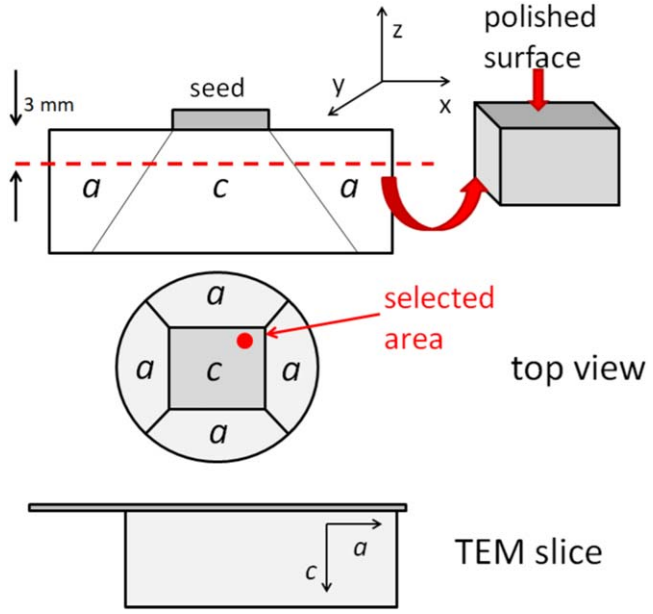


**Figure 2.** Schematic sketch of the original IG-YBCO pellet indicating the various growth sectors and the cut through the sample. The resulting surface was polished mechanically. The top view gives the final location where the TEM-slice was cut out. Finally, the sketch of the TEM slice gives the resulting crystallographic orientation of the investigated sample surface.

are indicated as well. The investigated sample area stems from the *c*-axis growth sector below the seed, slightly off the centre. Magnetisation data by SQUID magnetometry revealed a critical current density of $1.75 \times 10^5$ A cm$^{-2}$ at 77 K and self-field, as well as an irreversibiliy field larger than 5.5 T at 77 K.

The TEM slices for the TKD measurements were produced by focused-ion beam (FIB) milling in a dual-beam FIB workstation (FEI) using a routine allowing for reduced surface damage. The polished sample surface is covered by Pt to reduce the influence of charging effects. After lifting-off the TEM slice from the sample with the micromanipulator, the surface is ion-polished in a separate step by 2 keV Ga-ions to a thickness of about 80 nm. This step serves to further reduce the preparation damage of the surface area and for a further thinning of the sample to be transparent to the electron beam. Figure 1(c) presents a typical TEM slice after the completed ion-beam thinning process in a surface view (upper image) and its cross section (lower image). In figure 1(d), the TEM slice is shown ready for TKD investigations in the SEM chamber mounted on the sample holder for TKD. In figure 2, the location of the selected area for FIB-milling is presented, together with the final crystallographic orientation obtained for the milled-out TEM slice. As the FIB-milling takes place perpendicular to the original sample surface, all the following TKD investigations are, therefore, performed on an (*a*, *c*)-oriented surface of the original IG-YBCO sample.

### *2.2. Electron microscopy*

Figures 1(a) and (b) give schematic drawings of the arrangements for standard EBSD (=reflection mode) and TKD (=transmission mode). The primary electron beam hits the sample placed with an inclination towards the beam. After entering the sample, an electron cone is formed due to Bragg reflection at the crystal layers [27]. This electron cone is intercepted by a phosphor screen, where the Kikuchi patterns are recorded. TKD works with a transmitted electron beam, and the cones are formed from emanating electrons on the backside of the sample. Therefore, an electron-transparent sample is required for TKD.

TEM investigations were performed using a JEOL JSM-2011 transmission electron microscope operating at 200 kV with a $LaB_6$ cathode. The EBSD analysis was performed in a JEOL 7000F SEM microscope equipped with a TSL (TexSEM Labs, UT [28]) analysis unit. The Kikuchi patterns were generated at an acceleration voltage of 15 kV, and were recorded by means of a DigiView camera system. To produce a crystallographic orientation map, the electron beam was scanned over a selected surface area and the resulting Kikuchi patterns were indexed and analysed automatically, represents the common EBSD method working in reflection mode. Automated EBSD scans were performed with a step size down to 50 nm. For TKD, the TEM-slices were mounted in the SEM on a specially fabricated sample holder allowing for the correct 70° inclination of the sample required. The stage with the sample holder is inclined to an angle of −20°, which enables together with the sample mounting the same detector position to be used for the EBSD detector as in the standard configuration. Here, the electron beam is passing through the sample (transmission mode) and the electron cones are formed on the backside of the sample. The electron beam operates at 30 kV, and the working distance is set to 5 mm. The TKD stepsize was 5 nm. An image of the entire arrangement within the SEM chamber is presented in figure 1(d). To improve the imaging quality even further, the TEM slices were treated by additional low-angle (5°) argon ion-polishing (5 keV, 5 min). This process increases the image quality (IQ) of the resulting Kikuchi patterns as described in [29] for the investigation of ferrite samples, and removes mainly adhered particles on the surface, so only a minor surface layer of the slice is affected.

## 3. Results and discussion

Figure 3 shows various TKD mappings on the TEM slice prepared. Figure 3(a) is a SEM image taken in EBSD-conditions. The small IQ map shown in figure 3(a) is represented in the same scale, indicating the position of the following EBSD mappings. Figure 3(b) is a phase map with YBCO drawn in red and Y-211 particles in green. Figure 3(c) is a UGC map, which highlights the grains detected by EBSD using different colours. A comparison with the phase map (b) reveals directly that at many Y-211 grains also small grains of YBCO are formed. Figure 3(d) is a map of the grain-shape aspect ratio, which gives information on the shape of the grains. Finally, figure 3(e) is an IQ map with the misorientation boundaries highlighted in colour. The colour codes for maps (d) and (e) are indicated in between the maps.

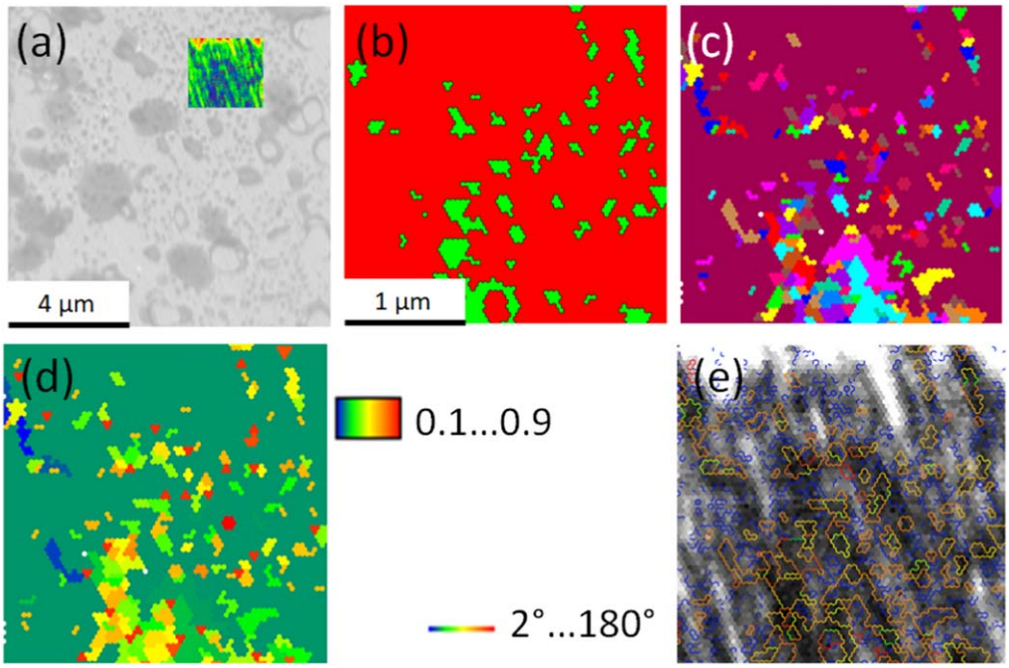


**Figure 3.** TKD mappings. (a) Is a SEM image indicating the position of the following TKD mappings. (b) Is a phase map (YBCO—red, Y-211—green), (c) is a UGC map, (d) is a map of the grain-shape aspect ratio, and (e) is a grey-scale IQ map with the misorientation boundaries highlighted in colour (2°–15°, 20°–55°, 60°–75°, 80°–125° and 130° and above). The colour codes for maps (d) and (e) are indicated in between the maps.

In total, 4524 boundaries are detected (misorientation larger than 2° is considered a boundary) with a total length of 104.5 $\mu$m. More details of the data obtained are discussed at figure 6 below.

Figures 4(a) and (b) present the orientation mappings (inverse pole figure or IPF maps) in the direction normal to the sample surface (normal direction (ND) or [001]) for YBCO (a) and Y-211 (b) separately. The respective other phase is drawn in black. The colour code for the maps is given in the stereographic triangle. Both phases are orthorhombic, and the ICDD datafiles no. #381433 and #752426 were employed for the indexation of YBCO and Y-211, respectively. It is obvious that the YBCO matrix shows a strong orientation, but also some distinct misorientations mostly located closely to the Y-211 grains. In contrast to this, the embedded Y-211 particles are more randomly oriented. In figure 4(c), we show a rainbow-coloured IQ map, together with the contours of the Y-211 particles indicated in white. The IQ values obtained range between 488 and 1202, which is quite high for a ceramic material. This mapping gives an impression of the distribution of the IQs of the Kikuchi patterns, and in a first approximation, an idea where the YBCO matrix may be strained. Here, we see that the present map shows the IQ values around the Y-211 particles being distinctly smaller than those of the remaining YBCO matrix. In previous publications, it was always speculated that the strain field within the YBCO matrix caused by the Y-211 particles may play an important role for the resulting flux pinning, so a measurement of the residual strain in the YBCO matrix is an important issue.

Measuring the strain with EBSD is possible as discussed in recent reviews [30–32], and a quantitative analysis is based on an evaluation of the IQ data of the Kikuchi patterns. The presence of strain clearly distorts the crystal lattice and thus, the observed Kikuchi patterns are deteriorated, leading to a reduction of the IQ values achieved. Therefore, the IQ mapping can give a first indication of the strain distribution within the YBCO matrix. From the mapping (c), we note that the areas of low IQ (blue) have a stripe-like character, and the Y-211 particles are arranged within these stripes. Areas including many Y-211 particles consequently show low IQ values. For large Y-211 grains, there is a much larger area with low IQ values around them as for other, tiny Y-211 particles, which indicates that the larger (or clustered) Y-211 particles are influencing the YBCO matrix much more as the tiny Y-211 particles.

However, for a proper investigation of the strain, the IQ-maps are not well suited as the IQ can be influenced by many other factors like grain boundaries and secondary phases, which is exactly corresponding to our present situation. The other factors influencing the IQ values like the camera settings, effects of sample surface preparation, etc, are not playing a large role in the present case of a small TEM slice being prepared by ion beams. A better way to visualise the strain distribution is the kernel average misorientation (KAM) mapping [30, 32]. In the literature, besides the classical deformation experiments KAM maps were already employed to study strain around embedded carbide particles in Ni superalloys [33], in SiGe thin films [34] and even in Ni/Ni-CNT nanoparticles [35].

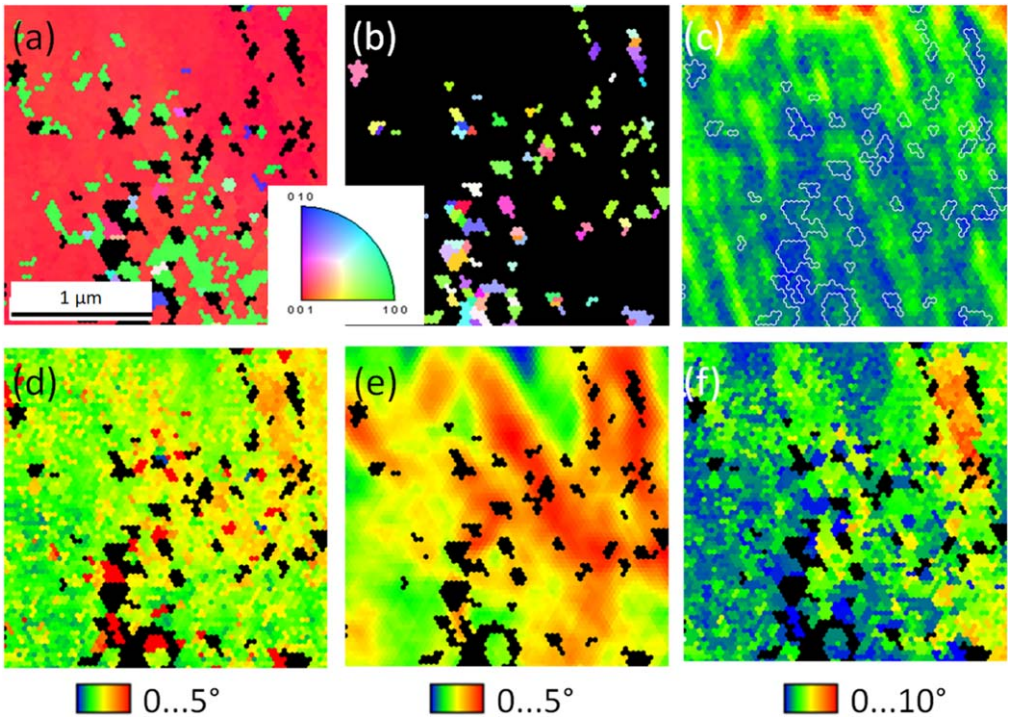


**Figure 4.** Inverse pole figure orientation mapping for YBCO (a) and Y-211 (b). The respective other phase is drawn in black. (c) Rainbow-coloured IQ mapping together with the contours of the detected Y-211 particles drawn in white. This gives an impression of the reduced image quality of the Kikuchi patterns around the embedded Y-211 particles. (d) Is the kernel average misorientation (KAM) map, (e) the local orientation spread and (f) the grain reference orientation deviation mapping. The colour codes are given below the maps. For maps (d)–(f), the Y-211 particles are represented in black. These maps reveal that the YBCO matrix shows misorientations of up to 10° in between the Y-211 particles.

Figure 4(d) presents such a KAM map (2nd neighbourhood—6 surrounding points to each pixel). Here, we see that the misorientation is largest in between the Y-211 particles, which are drawn here in black. This result is further manifested when looking at the mapping of the grain orientation spread presented in (e) and the grain reference orientation deviation mapping shown in (f).

The local strain in the YBCO matrix around the Y-211 particles must be partly so high that some small YBCO grains are created in close neighbourhood to the Y-211 particles in order to release the strain. A comparison of the YBCO-IPF map (a) and the KAM map (d) now reveals that the misoriented YBCO grains (coloured blue or magenta) are indeed located in the areas exhibiting the highest misorientation. The formation of such subgrains close to the Y-211 particles was already seen in earlier publications [36, 37]. The larger the embedded Y-211 particles, the more such YBCO subgrains are formed. The detailed investigation of strain created by embedded particles in the YBCO matrix will be a topic for future investigation as the strain fields created may act as additional flux pinning sites.

Figure 5 gives the pole figures for YBCO and Y-211 in ND corresponding to the IPF-mapping shown in figure 4. This clearly indicates the strong texture of the YBCO matrix, and the more random character of the Y-211 phase.

In figures 6(a)–(f), several EBSD-determined graphs concerning the grain properties are presented. The YBCO phase is always drawn using red, the Y-211 phase using blue

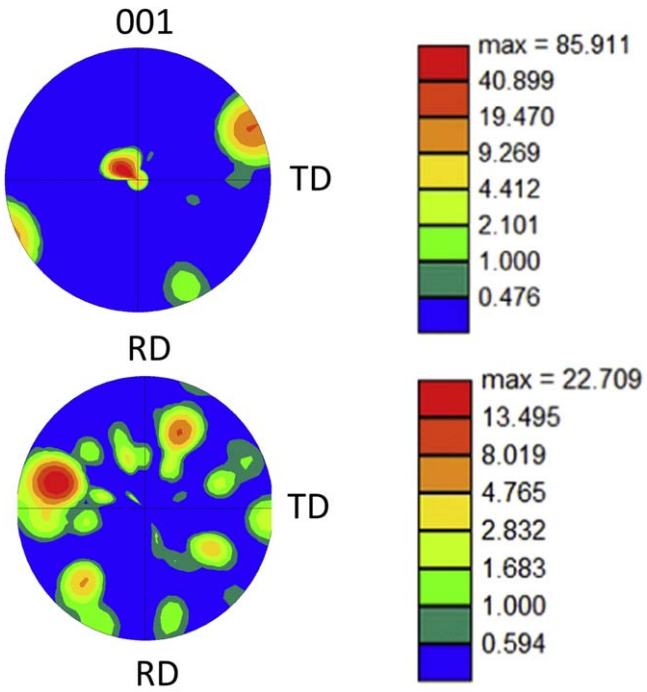


**Figure 5.** EBSD pole figures for YBCO (a) and Y-211 (b) in the direction normal (ND) to the sample surface.

colour. Figure 6(a) shows the grain size distribution for both phases. The Y-211 particles have sizes between 60 and 210 nm, so these particles are considerably smaller than most

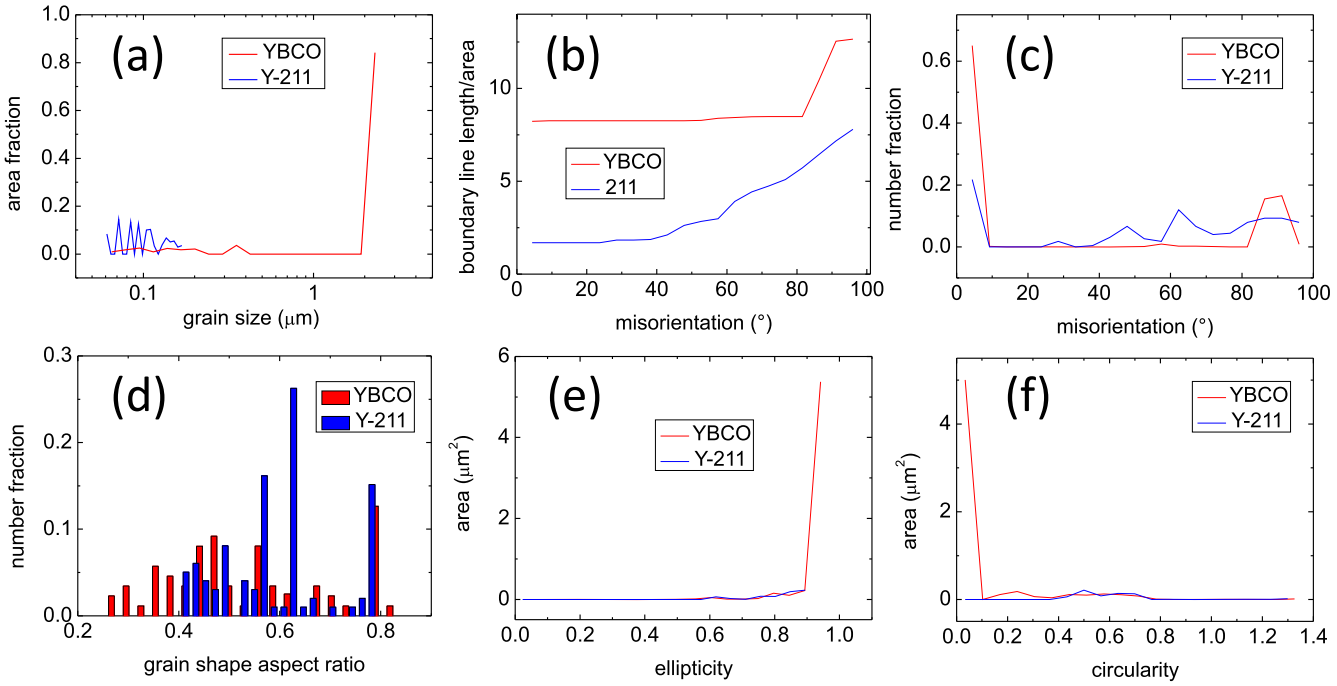


**Figure 6.** EBSD-determined graphs for the grain size (a), the boundary density (b), the misorientation angles (c), the grain-shape aspect ratio (d), the grain shape ellipticity (e) and the grain shape circularity (f). All data for YBCO are given in red, whereas Y-211 is drawn in blue.

of the Y-211 particles found in MTMG samples, even though refiners like Pt or $CeO_2$ were applied [38]. The small YBCO subgrains formed have similar sizes like the Y-211 particles, and the remainder of the sample is one large YBCO grain. The plot of figure 6(b) gives the grain boundary (GB) density in the investigated area. Here, we show the data for the two phases separately. The GB density for YBCO is nearly constant, with a sharp increase towards 90°, whereas the 211 phase exhibits an increasing GB density. Figure 6(c) shows the distribution of the GB misorientations, where YBCO shows a majority of low-angle GBs. The 211 phase has in contrast some GBs with angles between 40 and 60°, and a maximum at 70°. Figure 6(d) presents a plot of the GB aspect ratio of both phases. The grain shape aspect ratio is defined as the length of the minor axis, $a$, divided by the length of the major axis, $b$, of an ellipse fitted to a detected grain by the EBSD software. YBCO exhibits several large, elongated grains, while the 211 phase has a peak at ∼0.6. The Y-211 particles tend to be slightly more circular, i.e. with both axes being equally long. For both phases, the small grains have a grain size aspect ratio of 0.8. These phase-resolved analysis of the GB and grain properties corroborates the earlier results obtained on melt-textured bulk samples [36, 37].

The plots in figures 6(e) and (f) demonstrate details of the shape of the particles found here. The grain shape ellipticity is on the first approach similar to the aspect ratio and is given as $\sqrt{1-\frac{a^2}{b^2}}$. The grain shape circularity is a measure of the compactness of the grain. It is defined as $4\pi A/p^2$, where $A$ is the area of the grain and $p$ is the perimeter [28]. These data give additional information on the grain characteristics. The ellipticity (e) is similar for both YBCO and Y-211, whereas the circularity reveals differences between the two phases for low and high circularities.

As already mentioned, the formation of subgrains around the Y-211 particles embedded within the YBCO matrix was already seen in previous papers dealing with EBSD performed on melt-textured, melt-grown YBCO samples [36, 37], but on a different lengthscale using standard EBSD. This formation of subgrains is a direct consequence of the large strain around the Y-211 particles. The size of these YBCO subgrains is always smaller than that of the Y-211 particles. The present measurements reveal further that this high strain is also caused by the much smaller Y-211 particles obtained here, and the strain can be directly visualised using the KAM mappings of the YBCO phase. A further quantification of these data will be the next task, which is, however, complicated due to the more complex orthorhombic crystal structure of YBCO and Y-211.

Finally, figures 7(a)–(d) present several TEM images obtained from the same TEM-slice, taken with a magnification of 8000×. The Y-211 particles are clearly visible as slightly elliptic objects, which are clearly separated from the YBCO matrix by a GB. The Y-211 particles are densely packed with partly only a small distance between them. In images (a) and (d), Y-211 grains with grain boundaries between them are visible, which is also observed in the Y-211-IPF-map (figure 4(b)). The YBCO matrix reveals the presence of strain around the Y-211 particles as indicated by arrows. These observations demonstrate once more the big advantage of TKD as the TEM-slices can also be used for TEM imaging, although the exactly same location for investigation cannot straightforwardly be recovered in the different instrument.

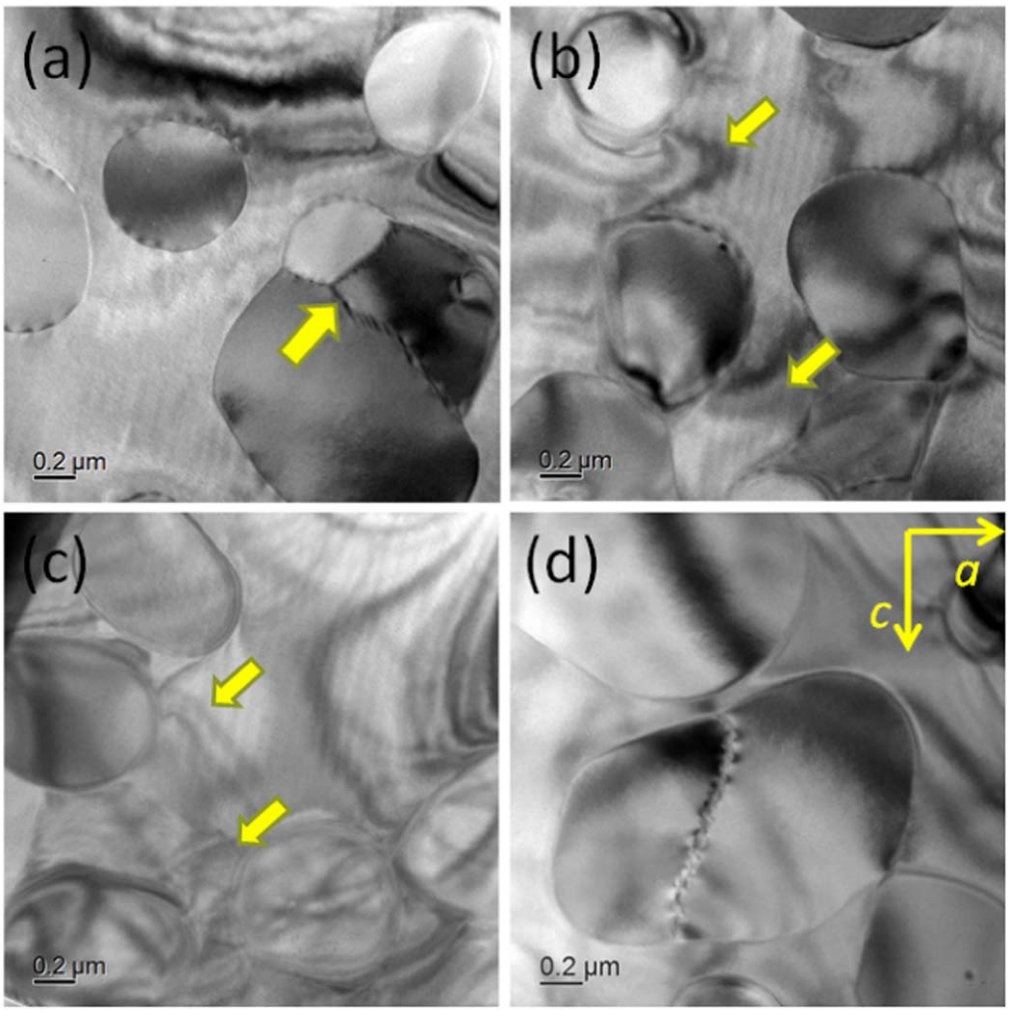


**Figure 7.** (a)–(d) TEM images taken on the same TEM-slice of the IG-processed YBCO sample, magnification 8000×. The arrows point to the effects of strain around the Y-211 particles embedded in the YBCO matrix.

The imaging of the strain field around the Y-211 particles represents an important step forward to better understanding of the flux pinning properties of the Y-211 particles. The strained YBCO matrix and the YBCO subgrains must also be considered when defining an effective radius for flux pinning in the melt-textured YBCO samples. The deeper analysis of the EBSD-data in form of graphs reveals a variety of details of the grain arrangement, a comparison of which may bring the design of an ideal microstructure for flux pinning even further. Therefore, the EBSD technique, and here especially the TKD technique for the analysis of nanometre-sized objects, is proven to be a very useful tool to provide better understanding of the specific microstructure of the IG-processed YBCO superconductors.

## 4. Conclusions

Transmission Kikuchi diffraction (TKD) was successfully carried out on TEM-slices prepared from IG-processed YBCO superconductor samples. The higher spatial resolution and the higher IQ obtained in the TKD measurements enabled the orientation measurements of the tiny Y-211 particles embedded within the YBCO matrix. The strain fields around the Y-211 particles were imaged using the average kernel miorientation mapping, which is an important step forward to better understanding of the resulting flux pinning properties. The analysis further showed details about the grain sizes, the misorientations, and the grain shape aspect ratio of the Y-211 grains. Together with the TEM images obtained from the same TEM-slices, a complete picture of the microstructure on the nanometre scale can be obtained, which enables the tailoring of the flux pinning properties of the IG-processed YBCO bulk samples.

## Acknowledgments

We thank M Muralidhar, K Nakazato (SIT, Tokyo) for the IG-processed YBCO sample studied here, and K Berger, B Douine and Q Nouailhetas (GREEN, Nancy, France) for valuable discussions concerning the possible applications of melt-textured superconductor materials. This work is part of the SUPERFOAM international project funded by ANR and

DFG under the references ANR-17-CE05-0030 and DFG-ANR Ko2323-10, respectively.

## ORCID iDs

A Koblischka-Veneva https://orcid.org/0000-0001-7409-671X
M R Koblischka https://orcid.org/0000-0003-4924-341X

## References

[1] Murakami M 1994 Melt-processing of high-temperature superconductors *Prog. Mater. Sci.* **38** 311–57
[2] Tomita M and Murakami M 2003 High-temperature superconductor bulk magnets that can trap magnetic fields of over 17 Tesla at 29 K *Nature* **421** 517–20
[3] Durrell J H *et al* 2014 A trapped field of 17.6T in melt-processed, bulk Gd–Ba–Cu–O reinforced with shrink-fit steel *Supercond. Sci. Technol* **27** 08200
[4] Buzdin A and Feinberg D 1996 Electromagnetic pinning of vortices by non-superconducting defects and their influence on screening *Physica* C **256** 303–11
[5] Kim C-J and Hong G-W 1999 Defect formation, distribution and size reduction of in melt-processed YBCO superconductors *Supercond. Sci. Technol* **12** R27–42
[6] Jeong I K, Kim D Y, Park Y K, Lee K W and Park J C 1991 Infiltration-reaction process for fabricating $YBa_2Cu_3O_{7-\delta}$ superconductor *Physica* C **185–189** 2393–4
[7] Iida K, Babu N H, Shi Y and Cardwell D A 2005 Seeded infiltration and growth of large, single domain Y–Ba–Cu–O bulk superconductors with very high critical current densities *Supercond. Sci. Technol* **18** 1421–7
[8] Devendra Kumar N, Rajasekharan T and Seshubai V 2013 Preform optimization in infiltration growth process: an efficient method to improve the superconducting properties of $YBa_2Cu_3O_{7-x}$ *Physica* C **495** 55–65
[9] Kumar N D, Rajasekharan T, Muraleedharan K, Banerjee A and Seshubai V 2010 Unprecedented current density to high fields in $YBa_2Cu_3O_{7-\delta}$ superconductor through nano-defects generated by preform optimization in infiltration growth process *Supercond. Sci. Technol* **23** 105020
[10] Devendra Kumar N, Rajasekharan T and Seshubai V 2013 Preform optimization in infiltration growth process: an efficient method to improve the superconducting properties of $YBa_2Cu_3O_{7-x}$ *Physica* C **495** 55–65
[11] Devendra Kumar N, Shi Y-H and Cardwell D A 2016 Fabrication of bulk (RE)BCO superconductors by the infiltration and growth process: past *Present and Future Superconductivity Applications Today and Tomorrow* ed M Muralidhar (New York: NOVA Science Publishers) ch 1, pp 1–35
[12] Namburi D K, Durrell J H, Jaroszynski J, Shi Y H, Ainslie M, Huang K Y, Dennis A R, Anthony R, Hellstrom E E and Cardwell D A 2010 A trapped field of 14.3T in Y–Ba–Cu–O bulk superconductors fabricated by buffer-assisted seeded infiltration and growth *Supercond. Sci. Technol* **23** 105020
[13] Humphreys F J 2004 Characterisation of fine-scale microstructures by electron backscatter diffraction (EBSD) *Scr. Mater.* **51** 771–6
[14] Dingley D 2004 Progressive steps in the development of electron backscatter diffraction and orientation imaging microscopy *J. Microsc.* **213** 214–24
[15] Chen D, Kuo J-C and Wu W-T 2011 Effect of microscopic parameters on EBSD spatial resolution *Ultramicroscopy* **111** 1488–94
[16] Koblischka M R and Koblischka-Veneva A 2013 Applications of the electron backscatter diffraction technique to ceramic materials *Phase Transit* **86** 651–60
[17] Trimby P W 2012 Orientation mapping of nanostructured materials using transmission Kikuchi diffraction in the scanning electron microscope *Ultramicroscopy* **120** 16–24
[18] Sneddon G C, Trimby P W and Cairney J M 2016 Transmission Kikuchi diffraction in a scanning electron microscope: a review *Mater. Sci. Eng.* R **110** 1–12
[19] Keller R and Geiss R 2012 Transmission EBSD from 10 nm domains in a scanning electron microscope *J. Microsc.* **245** 245–51
[20] Britton T B, Holton I, Meaden G and Dingley D 2013 High angular resolution electron backscatter diffraction: measurement of strain in functional and structural materials *Microsc. Anal.* **27** 8–13
[21] van Bremen R, Ribas Gomes D, de Jeer L T H, Ocelik V and De Hosson J T M 2016 On the optimum resolution of transmission-electron backscattered diffraction (t-EBSD) *Ultramicroscopy* **160** 256–64
[22] Koblischka-Veneva A, Koblischka M R, Schmauch J and Hannig M 2018 Human dental enamel: a natural nanotechnology masterpiece investigated by TEM and t-EBSD *Nano Res.* **11** 3911–21
[23] Wong D C K, Yeoh W K, Trimby P W, De Silva K S B, Bao P, Li W X, Xu X, Dou S X, Ringer S P and Zheng R K 2016 Characterisation of nano-grains in $MgB_2$ superconductors by transmission Kikuchi diffraction *Scr. Mater.* **101** 36–9
[24] Koblischka-Veneva A, Koblischka M R, Schmauch J, Inoue K, Muralidhar M, Berger K and Noudem J 2016 EBSD analysis of $MgB_2$ bulk superconductors *Supercond. Sci. Technol* **29** 044007
[25] Koblischka-Veneva A, Koblischka M R, Schmauch J and Murakami M 2019 Transmission-EBSD (t-EBSD) as tool to investigate nanostructures in superconductors *J. Supercond. Nov. Magn.* **32** 3155–63
[26] Nakazato K, Muralidhar M, Koshizuka N, Inoue K and Murakami M 2014 Effect of growth temperature on superconducting properties of $YBa_2Cu_3Oy$ bulk superconductors grown by seeded infilltration *Physica* C **504** 4–7
[27] Reimer L 1985 *Scanning Electron Microscopy: Physics of Image Formation and Microanalysis* (Berlin: Springer)
[28] TexSEM Laboratories (TSL). Orientation Imaging Microscopy Software V7.2, User Manual, TexSEM laboratories, (TSL), Draper, UT, 2015
[29] Koblischka-Veneva A, Koblischka M R, Schmauch J, Chen Y and Harris V G 2010 EBSD analysis of the microtexture of Ba-hexaferrite samples *J. Phys.: Conf. Ser.* **200** 082014
[30] Wright S I, Nowell M M and Field D P 2011 A review of strain analysis using electron backscatter diffraction *Microsc. Microanal.* **17** 316–29
[31] Wilkinson A J and Britton T B 2012 Strains, planes, and EBSD in materials science *Mater. Today* **15** 366–7
[32] Borrajo-Pelaez R and Hedström P 2017 Recent developments of crystallographic analysis methods in the scanning electron microscope for applications in metallurgy *Crit. Rev. Solid State Mater. Sci.* **43** 455–74
[33] Wilkinson A J, Britton T B, Jiang J and Karamched P S 2014 A review of advances and challenges in EBSD strain mapping *IOP Conf. Ser. Mater. Sci. Eng.* **55** 012020
[34] Vaudin M D, Osborn W A, Friedman L H, Gorham J M, Vartanian V and Cook R F 2015 Designing a standard for strain mapping: HR-EBSD analysis of SiGe thin film structures on Si *Ultramicroscopy* **148** 94–104

[35] Carneiro I, Viana F, Vieira M E, Fernandes J V and Simoes S 2019 EBSD analysis of metal matrix nanocomposite microstructure produced by powder metallurgy *Nanomaterials* **9** 878

[36] Koblischka-Veneva A, Koblischka M R, Mücklich F, Ogasawara K and Murakami M 2005 Interactions of $Y_2BaCuO_5$ particles and the YBCO matrix within melt-textured YBCO samples studied by means of electron backscatter diffraction *Supercond. Sci. Technol.* **18** S158–63

[37] Ogasawara K, Sakai N, Koblischka M R, Koblischka-Veneva A and Murakami M 2004 Effects of subgrains on critical current properties in melt-processed RE-Ba–Cu–O bulk superconductors *Supercond. Sci. Technol.* **17** S61–5

[38] Murakami M, Fujimoto H, Yamaguchi K, Nakamura N, Koshizuka N and Tanaka S 1992 Is $Y_2BaCuO_5$ inclusion effective pinning site in $YBa_2Cu_3O_7$? *J. Adv. Sci.* **4** 75–8